Modelling entrainment volume due to surface-parallel vortex interactions with an air–water interface

Citation: Hendrickson K, Yu X, Yue DKP. Modelling entrainment volume due to surface-parallel vortex interactions with an air–water interface. Journal of Fluid Mechanics. 2022;938:A12.

As Published: 10.1017/jfm.2022.144

Publisher: Cambridge University Press

Persistent URL: https://hdl.handle.net/1721.1/155740

Version: Author's final manuscript: final author's manuscript post peer review, without publisher's formatting or copy editing

Modeling entrainment volume due to surface-parallel vortex interactions with an air-water interface

K. Hendrickson†, Xiangming Yu and Dick K.P. Yue

Department of Mechanical Engineering, Massachusetts Institute of Technology, Cambridge, MA 02139, USA

(Received xx; revised xx; accepted xx)

We consider the entrainment volume that results from the quasi two-dimensional interactions of rising surface-parallel vorticity with an air-water interface. Based on systematic (three-dimensional) direct numerical simulations (DNS) of the canonical problem of a rectilinear vortex pair impinging on and entraining air at the free surface, we develop a phenomenological model to predict the resulting entrainment volume in terms of four key parameters. We identify a new parameter, a circulation flux Froude number $Fr^2_\Xi = |\Gamma|W/a^2 g$, that predicts the dimensionless volume $\forall$ of entrained air initiated by a coherent vortical structure of circulation Γ, effective radius a, vertical rise velocity W with gravity g. For Fr^2_Ξ below some critical value $Fr^2_{\Xi cr}$, no air is entrained. For $Fr^2_\Xi > Fr^2_{\Xi cr}$, the average initial entrainment $\overline{\forall}_o$ scales linearly with $(Fr^2_\Xi - Fr^2_{\Xi cr})$. We also find that $\overline{\forall}_o$ is linearly dependent on circulation Weber number We_Γ for a range of vortex Bond number $5 \lesssim Bo_\Gamma \lesssim 50$, and parabolically dependent on circulation Reynolds Re_Γ for $Re_\Gamma \lesssim 2580$. Outside of these ranges, surface tension and viscosity have little effect on the initial entrainment volume. For the canonical rectilinear vortex problem, the simple model predicts $\overline{\forall}_o$ extremely well for individual coherent structures over broad ranges of Fr^2_Ξ, We_Γ, Bo_Γ and Re_Γ. We evaluate the performance of this parameterization and phenomenological entrainment model for air entrainment due to the complex periodic vortex shedding and quasi-steady wave breaking behind a fully-submerged horizontal circular cylinder. For the range of parameters we consider, the phenomenological model predicts the event-by-event dimensionless entrainment volume measured in the DNS satisfactorily for this complex application.

Key words:

1. Introduction

There are many possible mechanisms for entrainment observed at an air-water interface including four main processes: direct entrapment from droplet impacts and plunging breaking waves (e.g., Tran *et al.* 2013; Deane & Stokes 2002), plunging jets that entrain via the

† Email address for correspondence: khendrk@mit.edu

shear layer and/or jet surface disturbances (e.g., Biń 1993), surface aeration and surface roller-bores (e.g., Leng & Chanson 2019; Ezure *et al.* 2011), and surface normal and tangential vortices interacting with the interface. Our interest is the latter mechanism of air entrainment due to interaction of coherent vorticity with the free surface. Specifically, recent numerical (Yu *et al.* 2019*b*; Masnadi *et al.* 2019) and experimental (André & Bardet 2017) investigations of strong free-surface turbulent flows identify tangential (i.e. surface-parallel) vortex structures interacting with an interface (and the associated near-surface vortex instabilities/transformations) as an important mechanism for air entrainment. These three-dimensional vortex structures generally possess local quasi-two dimensional regions (such as a segment of a vortex ring or the top of a horseshoe vortex structure) tangent to the free surface interface and interact with it. Such originating vortex-interface interactions can be viewed as a macroscopic entrainment event mechanism (Castro *et al.* 2016). Using this macroscopic event framework, our interest is the development of a simple yet robust entrainment model to predict the total volume of entrained air due to strong quasi two-dimensional, surface-parallel vorticity interactions with the air-water interface.

The detailed interaction of horizontal (surface-parallel) vortices with a free surface in the absence of entrainment is well documented (see Appendix A). Sarpkaya & Suthon (1991) experimentally determined that surface-parallel vortex pairs rising towards and interacting with an interface create a local depression (or a scar). Ohring & Lugt (1991) and Yu & Tryggvason (1990) investigated an equivalent two-dimensional problem using numerical simulations and found similar local surface deformations and ultimately identified gravity, surface tension, and geometrical parameters as the main parameters influencing the interaction of the vortex pairs with the interface. While entrainment was not considered in these and many subsequent studies, they do suggest the potential for entrainment to occur. Within a macroscopic entrainment event framework, if such vortex interactions are strong enough to overcome the stabilizing effects of gravity and surface tension, such interactions eventually lead to entrainment. While the detailed interactions (eventually) involve well-documented three-dimensional vortex instabilities (e.g., Sarpkaya & Suthon 1991; Dommermuth 1993; André & Bardet 2017), our hypothesis is that a simple phenomenological model based on the (macroscopic) parameters of the underlying quasi-two-dimensional surface-parallel coherent vorticity may be able to predict the total entrainment volume (per unit length in the dominant direction) without explicitly describing the details of the complex vortex breakup and entrainment mechanisms.

Macroscopic entrainment modeling for turbulence-interface interactions initially introduced by Baldy (1993) assumes that the air entrainment is linearly related to the turbulence dissipation (through similarity arguments). More recent versions of this model propose a volumetric entrainment source proportional to turbulent dissipation and use experimentally measured bubble distributions to populate entrained bubble models (Ma *et al.* 2011; Derakhti & Kirby 2014). The volume source entrainment model of Castro *et al.* (2016) begins with the model of a single vortex of given strength and distance from the interface and builds a probabilistic model to determine an entrainment rate and bubble distribution. All of these models relate the rate of air entrainment to the underlying turbulent field (through local dissipation and vorticity) with modest success. However, all of these models rely on a certain amount of empiricism and assumptions that have yet to be confirmed by experiments. As yet, it is not clear what key surface-parallel vorticity characteristics (and to what degree they need to be resolved) are critical for predicting if, where, and how much entrainment will occur. This understanding is critical for large-scale computational applications such as the complex air-water flows in the near-wake behind surface ships where fully-resolved turbulent-interface interactions is infeasible (e.g. Hendrickson & Yue 2019*b*; Castro *et al.* 2016; Drazen *et al.* 2010; Wyatt *et al.* 2008; Fu *et al.* 2006).

In this paper, we focus on developing a simple entrainment model based on our macroscopic entrainment event framework. We investigate entrainment initiated by coherent vortex structures with a locally surface-parallel dominant direction. We perform three-dimensional direct numerical simulations (DNS) of the incompressible, two-phase (air-water) Navier-Stokes equations on a three-dimensional Cartesian grid using a conservative volume-of-fluid (cVOF) method (Weymouth & Yue 2010). To elucidate the basic underlying mechanism and parameter dependencies, we first consider the canonical problem of air entrainment by horizontal rectilinear vortices of known circulation Γ, radius a, rising towards the air-water interface with vertical velocity W. We perform systematic DNS over a broad range of parameters (Γ, a, W, surface tension σ, gravity g, and water kinematic viscosity $\nu_w = \mu_w/\rho_w$) and measure the entrainment volume $\mathcal{V}_e$. Using this extensive DNS dataset, we identify the key dimensionless parameters relating the macroscopic vortex-interface interaction and the measured entrainment. We find that the most important parameter governing the initial dimensionless entrainment volume $\overline{\forall}_o$ is the circulation flux Froude number $Fr_\Xi^2 = \Xi/g$, which measures the relative strength between the circulation flux $\Xi = |\Gamma|W/a^2$ and gravity. The remaining key parameters we identified are the vortex Reynolds number Re_Γ, Weber number We_Γ and relative depth z_c/a below the interface at which these parameters are defined. We then use a representative subset of the DNS to develop an explicit model based on this parameterization. This model predicts the initial dimensionless entrainment volume extremely well when assessed across the entire scope of parameters of the DNS cases. Finally, we assess the validity of the entrainment model for a more complex problem of air entrainment due to periodic (plunging) quasi-steady wave breaking in the wake of a fully-submerged horizontal circular cylinder in a uniform inflow. For the range of parameters considered, our model predicts the event-by-event entrainment measured in the cylinder problem DNS satisfactorily for this complex problem. The modest success of the model to generalize from a simple test problem to this more complex flow demonstrates that we have identified the key dimensionless parameters that predict the onset, general location and quantity of a (macroscopic) entrainment event for surface-parallel vortex interactions.

The outline of this paper is as follows. Section 2 defines relevant quantities that describe the general interaction of a surface-parallel coherent structure with an interface. Section 3 details the direct numerical simulations of the canonical problem of rectilinear vortex tube-interface interactions. Section 4 identifies the set of parameters, including the circulation flux Froude number, and summarizes the new phenomenological entrainment model. Section 5 assesses the model for the periodic breaking behind a fully-submerged cylinder in a constant inflow. Section 6 concludes the paper with a summary and discussion of our findings. The appendix summarizes the salient features of air-entraining rectilinear vortex approaching a free surface (comparing to non-entraining cases).

2. Air entrainment due to interaction of surface-parallel vorticity with an interface

2.1. *Definitions*

Consider a general surface-parallel coherent vortex structure approaching an air-water interface. Macroscopically, the coherent structure approaches the interface and interacts with it in a manner that ultimately results in the entrainment of a volume of air $\mathcal{V}_e$. The coherent structure has volume V_Γ, circulation Γ, effective cylindrical radius a and a local orientation that is surface parallel (see figure 1(a)). The bulk fluid (water) has density and kinematic viscosity ρ_w and μ_w, and σ represents the surface tension coefficient of the air-water interface. The coherent structure geometric centroid $\mathbf{x_c}$=(x_c, y_c, z_c) and vertical rise

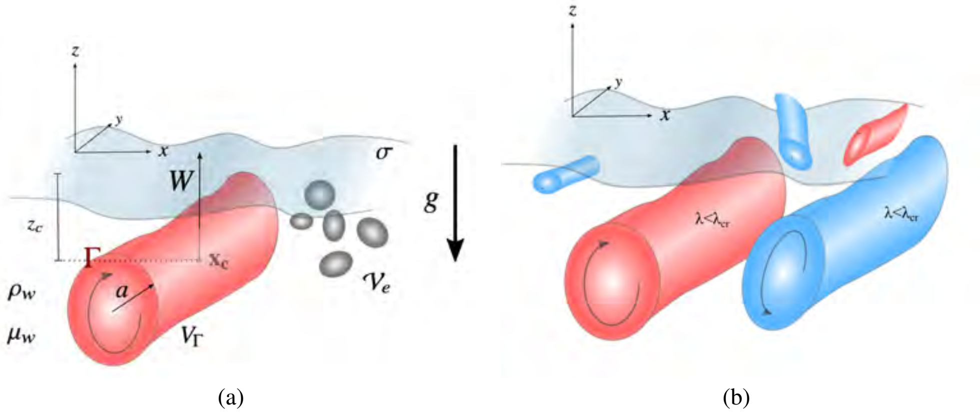

Figure 1: Schematic of (a) a general, surface-parallel coherent vortex structure rising towards the air-water interface and entraining air and (b) a general set of coherent structures that satisfy the criteria $\lambda < \lambda_{cr}$.

velocity W strongly influence the subsequent surface interactions and deformations (e.g Yu & Tryggvason 1990; Ohring & Lugt 1991; Lugt & Ohring 1992). Based on these given parameters, we write the following parameterization:

$$\mathcal{V}_e = f(a, \Gamma, \nu_w = \mu_w/\rho_w, g, \sigma/\rho_w, W, V_\Gamma, z_c)\,. \tag{2.1}$$

2.2. *Coherent structure identification*

To identify the geometric parameters of a coherent vortex structure as input to the model, we construct a scalar value of the $\lambda_2(\mathbf{x})$ eigenvalue (Jeong & Hussain 1995) as it provides a robust (albeit imperfect) mechanism to spatially identify the location and orientation of a coherent structure in an eigenplane across a vortex. We employ the Informed Component Labeling method (ICL) (Hendrickson *et al.* 2020) to identify the connected regions that satisfy the criterion $\lambda_2 < \lambda_{cr}$. ICL provides a method to identify the regions in the domain that satisfy $\lambda_2 < \lambda_{cr}$ and for each region, determine its volume $V_{\lambda 2}$, centroid location $\mathbf{x_c}$, extent in each Cartesian direction, and integrated quantities within the volume. With the coherent volumes identified in this manner (see figure 1(b)), we define the geometric quantities of interest as the vortex volume $V_\Gamma \equiv V_{\lambda 2}$, the length in the dominant direction L_d which is the largest extent measured by ICL, the cross-sectional area normal to that dominant direction $A_d = V_{\lambda 2}/L_d$, and an effective radius $a_{\lambda 2} = \sqrt{A_d/\pi}$. We compute circulation Γ and circulation flux Ξ of the vorticity component in that dominant direction ω_d using the local vertical velocity w by:

$$\Gamma = \frac{1}{L_d}\int \omega_d \, dV_{\lambda 2}\ ; \quad \Xi = \frac{1}{V_{\lambda 2}}\int |\omega_d| w \, dV_{\lambda 2}\ . \tag{2.2}$$

This method is geometrically simpler than the method of Masnadi *et al.* (2019), which uses the Q-criterion (Hunt *et al.* 1988) and constructs a spine of the coherent structure and estimates the vorticity and circulation on isoplanes perpendicular to the spine. Our method is robust and well suited for vortex structures with a clearly defined dominant direction such as those considered in this study. In the following section, $\lambda_{cr} = 0$ as defined by Jeong & Hussain (1995). We note that the λ_2 criterion suffers slightly when several vortices exist locally (Jeong & Hussain 1995) and it is common practice for more complex flows (e.g. §5) to select values $|\lambda_{cr}| > 0$ for visualization purposes. In §5, we discuss non-zero values of λ_{cr} and their influence on the performance of the model developed in §4.

3. Air entrainment due to surface-parallel vortex approaching an interface

To quantify the dependence of air entrainment on the coherent vortex properties and other physical parameters, we choose a simple canonical problem of a rectilinear surface-parallel vortex tube rising towards the interface with an initially known rise velocity. This is a well-studied problem in the absence of entrainment (e.g., Sarpkaya 1996; Sarpkaya & Suthon 1991; Yu & Tryggvason 1990; Ohring & Lugt 1991; Dommermuth 1993), and the main conclusions in this body of work relevant to our study are that gravity and the vortex geometric parameters (depth, size, and strength) control the interaction of the vortex with interface and that strong surface tension suppresses the surface curvature and formation of secondary surface vorticity.

For this canonical problem, we perform high-resolution (three-dimensional) DNS of the two-phase, incompressible Navier-Stokes equations with a fully-nonlinear interface using the conservative Volume of Fluid method (cVOF) (Weymouth & Yue 2010). The three-dimensional, two-phase incompressible Navier-Stokes equations in a single-fluid form with variable density ρ and viscosity μ are,

$$\begin{aligned}
&\frac{\partial \mathbf{u}}{\partial t} + \nabla\cdot(\mathbf{u}\mathbf{u}) = -\frac{1}{\rho}\nabla p + \frac{\mathbf{g}}{Fr^2} + \frac{1}{Re}\frac{1}{\rho}\nabla\cdot\tau + \frac{1}{We}\kappa\delta_s\mathbf{n}\,,\\
&\qquad\qquad \nabla\cdot\mathbf{u} = 0\,,\\
&\frac{\partial f}{\partial t} + \mathbf{u}\cdot\nabla f = 0\,,
\end{aligned} \tag{3.1}$$

where $f(\mathbf{x}, t)$ represents the volume fraction implemented by cVOF that enables robust and conservative transport of the gas-liquid interface. In (3.1), the volume fraction f provides the density and viscosity via $\rho(f) = f + (1-f)\rho_a/\rho_w$, $\mu(f) = f + (1-f)\mu_a/\mu_w$; $\mathbf{u}$ is the three-dimensional velocity field, p the total pressure field, $\mathbf{g}$ the unit vector in the direction of gravity, τ the variable viscosity stress tensor, δ_s the interfacial Dirac delta function, κ the interface curvature, and $\mathbf{n}$ the normal vector to the interface. The equation is non-dimensionalized by characteristic velocity scale U and length scale L and water density ρ_w and viscosity μ_w.

The numerical implementation of (3.1) is a second-order (in space and time) finite-volume scheme utilizing a staggered grid. Time integration is a two-stage Runge-Kutta method. We employ a projection method to conserve mass and solve for the pressure. The resulting variable coefficient Poisson equation is solved using the HYPRE library (Falgout *et al.* 2006). Finally, surface tension effects are implemented through the continuous surface force (CSF) method (Brackbill *et al.* 1992) along with a height-function method for the interface curvature (Popinet 2009, 2018). Details of the formulation and validations of the numerical method are available in Campbell *et al.* (2016); Yu *et al.* (2019*a*).

To create a known rise velocity for the vortex tube, we simulate a rectilinear surface-parallel vortex tube pair initially submerged below the air-water interface with initial radius a_0, spacing ℓ, vorticity scaling ω_c, circulation $\Gamma_0 = \pi a_0^2\omega_c$ and orientation angle Θ with the x-axis (see figure 2). We non-dimensionalize the problem with $L = a_0$ and $U = \Gamma_0/a_0$ such that the simulation parameters in (3.1) are $Fr^2 = \Gamma_0^2/ga_0^3$, $Re = \Gamma_0/\nu_w$, and $We = \Gamma_0^2\rho_w/a_0\sigma$. The density and viscosity ratios are respectively $\rho_a/\rho_w = 0.001$ and $\mu_a/\mu_w = 0.01$. The Cartesian domain size is (L_x, L_y, L_z)=$(L_x, 15, 30)a_0$ with water depth $H_w = 20a_0$. The domain width L_x varies depending on orientation angle. When $\Theta = 0$, $L_x = 30a_0$ and we

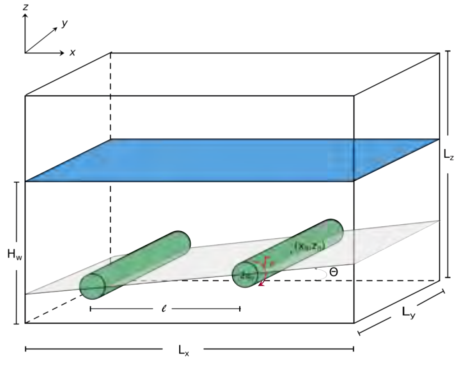

Figure 2: Schematic of a horizontal vortex pair rising towards the air-water interface with definitions for DNS

simulate only half of the vortex pair with a symmetry plane located at $x = 0$ and measure the entrainment volume based on the single vortex tube in the water. When $\Theta > 0$, $L_x = 60a_0$ and we simulate the pair of vortices and measure the entrainment volume based on the first vortex interaction with the surface. The remaining boundary conditions are symmetry planes in the z direction and periodic in the y direction.

We use (constant) grid spacing $\Delta = 15a_0/128$. Increased resolution of up to (constant) $\Delta = 15a_0/480$ was required for large Re and small We to provide adequate resolution of the laminar viscous free-surface boundary layer (Klettner & Eames 2012) and the relatively small entrainment volume at small We. Based on these grid sizes, the cell Bond number $Bo_\Delta = g\Delta^2\rho_w/\sigma$, which governs entrainment volume (Yu *et al.* 2019*b*; Yu 2019), are fully resolved. Grid sensitivity analyses determined that increasing the grid resolution beyond these reported values resulted in a less than 1% relative change in entrained volume, which is the objective of our simulations. The most grid sensitive aspect of these simulations is the surface connectivity between cells that influences the average entrainment measurements, which we address in §3.1. We note that if the full details of the small-scale capillary interactions are of interest, conditions such as the cell Weber number $We_\Delta \ll 1$ (Popinet 2018) may be relevant.

We initialize the DNS by assuming a Gaussian core vorticity distribution with $\omega_y/\omega_c = e^{(\mathbf{x}-\mathbf{x}_0)\cdot(\mathbf{x}-\mathbf{x}_0)/a_0^2}$, where $\mathbf{x}_0$ is the initial vortex core location. We solve for the one-dimensional vector stream function ψ that satisfies $\nabla^2\psi = -\omega_y$ using the same boundary conditions as the simulation. We solve the resulting indeterminate problem up to $\psi + const$ to determine the initial velocity field $\mathbf{u} = \nabla \times \psi$. To construct an initial condition that reduces any initial impulse on the free surface, we include the image vortices located in the air when constructing the initial vorticity field. For cases when $\Theta > 0$, we construct the water vortex pair such that the vortex closest to the surface is located at z_0.

We considered over a 100 DNS of rising vortex pairs covering a broad range of simulation parameters: $90 \lesssim Fr^2 \lesssim 2600$, $150 \lesssim Re \lesssim 2520$, $90 \lesssim We \lesssim \infty$ and $0 \leqslant \Theta \leqslant \pi/2$ focusing mainly on entraining cases. Our interest is macroscopic quasi two-dimensional processes, and we design the simulations to avoid three-dimensional instabilities using the following ideas. First, we set a shallow initial depth of the vortex pair z_0 to suppress long-wavelength instabilities that arise from vortices translating/interacting over long distances (Crow 1970; Sarpkaya & Suthon 1991). Second, we only consider vortices of within size range $0.1 \leqslant a_0/\ell \leqslant 0.3$ to limit short-wavelength instabilities (Widnall 1975; Sarpkaya & Suthon 1991). Combined with the periodic boundary conditions in the y direction, we expect the initial vortex pair approach to the surface and initial interaction to be effectively

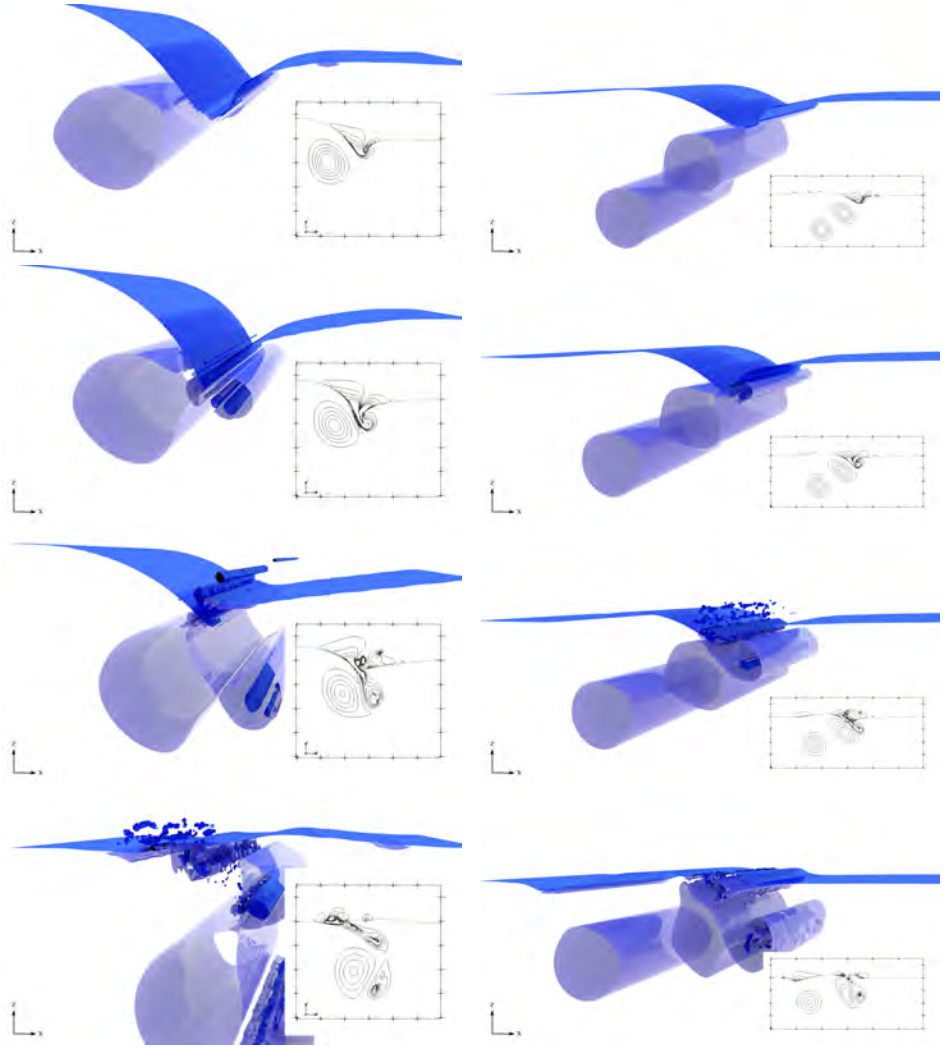

Figure 3: Visualization of two sample DNS simulation results. Blue isosurface f=0.5, purple $\lambda_2 = -0.01$ for $f \geqslant 0.5$, with inset a representative vertical plane with ω_y vorticity contours. (left) ℓ/a_0=5, Fr^2=790, $Re = 628$, $We = \infty$ and $\Theta = 0$ with vorticity contour details shown in figure 11a; (right) ℓ/a_0=5, Fr^2=494, $Re = 628$, $We = \infty$ and $\Theta = \pi/4$ with vorticity contour details shown in figure 13.

two dimensional. A detailed discussion of the vorticity and vortex core paths from these simulations appears in Appendix A, where we confirm the expected behavior of the vorticity in non-entraining cases and highlight the differences when entrainment occurs.

Generally, the surface-parallel vortex pair rises towards the interface causing the surface to deform as shown for two representative cases in figure 3. This deformation and the presence of viscosity induces a secondary vorticity of opposite sign in the water at the interface as well as a horizontal velocity component (Orlandi 1990; Ohring & Lugt 1991; Yu 2019). Depending on the parameters Fr^2, We and Re, entrainment occurs. As seen in figure 3, the initial entrainment event is essentially a two-dimensional process (as designed to provide the macroscopic modeling framework). As a result, the entrainment consists of almost uniform

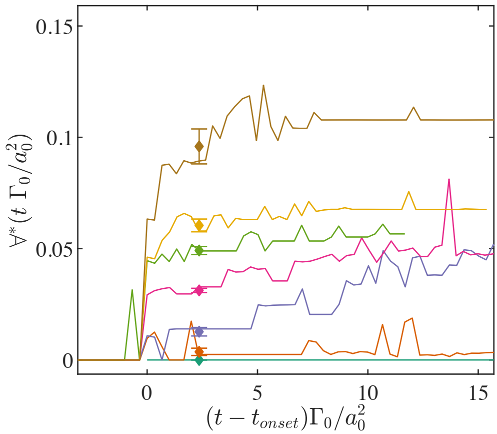

Figure 4: Instantaneous non-dimensional total entrainment volume $\forall = \mathcal{V}_e/L_y\pi a_0^2$ as a function of Froude number Fr^2 with Re=628, $We = \infty$, and ℓ/a_0=5. ♦ with error bars represent calculated average initial entrainment $\overline{\forall}_o = \overline{\mathcal{V}_e^o}/L_y\pi a_0^2$ with 95% confidence level.
Fr^2=(—— 99;—— 148;—— 197;—— 395;—— 493;—— 592;—— 790).

cylindrical tubes of air that become nonuniform and form smaller air cavities later in the entrainment process.

3.1. *Quantification of the entrainment volume*

We measure the total entrainment volume from the air volume fraction $(1 - f)$ using ICL as a two-level connected component algorithm, with the established optimum levels of $\theta = (0.4, 0)$ (Hendrickson *et al.* 2020). Figure 4 shows a sample of the measured total entrainment volume as a function of time for a series of Fr^2. As seen in this figure, the total entrainment volume can fluctuate as grid resolution influences the connectivity between cells in numerical simulations (Chan *et al.* 2021). In order to quantify the initial entrainment volume $\mathcal{V}_e^o$, we first define the onset time (t_{onset}) as the time where the entrained air volume exceeds and maintains a value above a threshold value of $O(10^{-5})$. We then sample the total entrained volume over a set of increasingly longer time periods from 0.25 to 1.5 vortex turnover times. The average initial entrainment volume $\overline{\mathcal{V}_e^o}$ represents the sample with the smallest standard deviation in that time period. Typically, the sample period is 1 or 1.5 vortex turnover times. In all subsequent plots, the error bars are the 95% confidence level of this average value.

3.2. *General scaling observations*

We performed DNS over a range of simulation parameters (Fr^2, Re, We) and vortex parameters (a_0, ω_c and Θ). Prior to presenting the model, we first describe three key observations (Yu 2019) using representative data in figure 5 to illustrate these trends. First, we observe a strong dependence of $\overline{\forall}_o$ on Re that then decreases for larger Re. For $Fr^2 = 790$, figure 5(a) shows this transition occurring at $Re \approx 1500$ with the average initial entrainment volume not increasing significantly for $Re \gtrsim 2000$. Second, we observe similar behavior between $\overline{\forall}_o$ and We where there is a strong dependence that then becomes less significant at large We. Across the entire DNS dataset, we determined that $\overline{\forall}_o$ is independent of We for $Bo = We/Fr^2 \gtrsim 50$. For $Bo \lesssim 50$, we observe a linear relationship $\overline{\forall}_o \propto We$ above a critical value We_{cr} as shown in figure 5(b). This critical value corresponds to the minimum

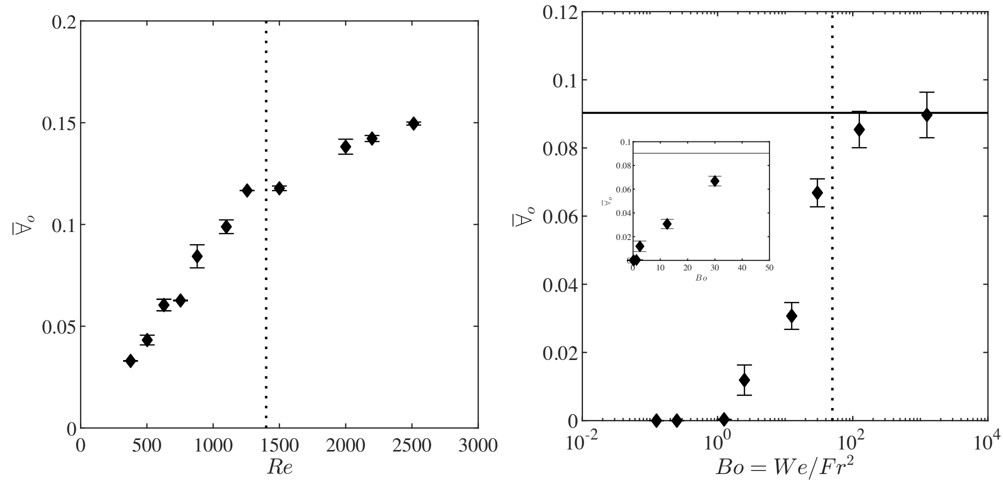

(a) Fr^2=790 and $We = \infty$.

(b) Fr^2=790 and Re=628

Figure 5: Average initial dimensionless entrainment volume $\overline{\forall}_o = \overline{\mathcal{V}_e^o}/L_y \pi a_0^2$ as a function of (a) Re and (b) Bo. In (b), — is $\overline{\forall}_o$ for $We = \infty$, inset linear axis.

Weber number to entrain air, which we determine to be $Bo \sim 1-2$ as expected. Finally, we note that in the absence of surface tension effects there is a similar critical Fr^2 value above which entrainment occurs (cf. figure 4). This critical Froude number, which we find to be $Fr^2 \sim 138$ for $Re = 628$, compares to the simulations of Yu & Tryggvason (1990) and Ohring & Lugt (1991) (after converting to equivalent length and velocity scales).

4. Parameterization and modeling of entrainment volume due to interaction of surface-parallel vorticity with an air-water interface

4.1. *Parameterization*

After extensive analysis of the DNS data from the vortex pairs in §3, we identify the key parameters that govern the average initial dimensionless entrainment volume $\overline{\forall}_o$. The parameterization we obtain reads:

$$\overline{\forall}_o \equiv \frac{\overline{\mathcal{V}_e^o}}{V_\Gamma} = f\left(Fr_\Xi^2 = \frac{|\Gamma|\, W}{a^2\, g}, We_\Gamma = \frac{\Gamma^2}{a(\sigma/\rho_w)}, Re_\Gamma = \frac{|\Gamma|}{\nu_w}, \frac{z_c}{a}\right). \tag{4.1}$$

The last three parameters are well established as being relevant to vortex interactions with an interface (e.g., Yu & Tryggvason 1990; Ohring & Lugt 1991): the vortex Weber number We_Γ measures the effect of surface tension, the vortex Reynolds number Re_Γ viscous effects, and z_c/a is the (centroid) depth relative to its effective radius a at which these parameters are quantified. The key new parameter we identify is the circulation flux Froude number Fr_Ξ^2 which measures the magnitude of the circulation flux density $\Xi = |\Gamma|\, W/a^2$ relative to gravity g. The sign of the circulation Γ is not relevant for Ξ (or Re_Γ) and we define Fr_Ξ^2=Ξ/g for $\Xi > 0$ and Fr_Ξ^2=0 for $\Xi < 0$ since we are only concerned with rising vorticity $W > 0$. The circulation Bond number is defined as $Bo_\Gamma = ga^2\rho_w/\sigma$. These model parameters are calculated using the coherent structure identification in §2.2 and (2.2) with λ_{cr}=0. In particular, $V_\Gamma = V_{\lambda 2}$ and $a = a_{\lambda 2}$. We propose a simple predictive model based on (4.1) by

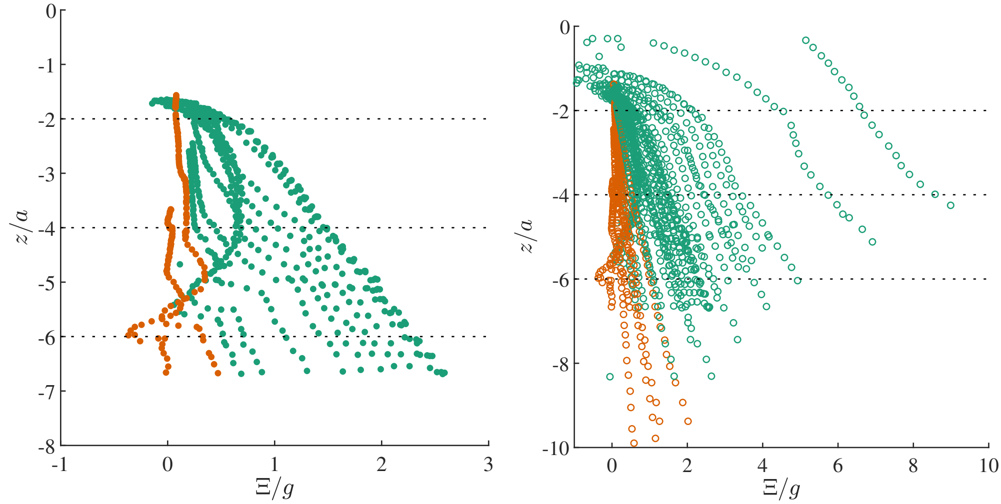

(a) ● $\overline{\forall}_o > 0$; ● $\overline{\forall}_o = 0$ (b) ○ $\overline{\forall}_o > 0$; ○ $\overline{\forall}_o = 0$

Figure 6: Ξ/g as a function of z_c/a for (a) variable Θ at fixed Fr^2, Re, and $We = \infty$ and (b) a range of Fr^2, Re, We, Γ_0 and a_0. In (a) Θ=0 (far right) to Θ=$\pi/2$ (far left).

assuming that the functional dependencies therein are separable, and write:

$$\forall^m = \mathcal{F}\left(Fr_\Xi^2; \frac{z_c}{a}\right)\mathcal{W}\left(We_\Gamma; \frac{z_c}{a}\right)\mathcal{B}\left(Re_\Gamma; \frac{z_c}{a}\right). \tag{4.2}$$

Equation (4.2) with the explicit dependencies of the parameters on the depth z_c/a acknowledges that the parameter values change with the evolving vortex structure as it approaches the interface.

4.2. *Circulation Flux*

Figure 6(a) shows Ξ/g as a function of relative distance to the static waterline z_c/a for a set of cases with variable Θ. For entraining cases, we show data for $t < t_{\text{onset}}$. For many oblique rise angles, Ξ/g varies linearly with depth providing that $z_c/a < -4$. For $z_c/a > -4$, the circulation flux depth dependence becomes more complex due to the interaction with the interface. We note here that for $\Theta = \pi/2$, the actual vortex motion is effectively horizontal and the implied rise towards the surface is due to the increase in a due to diffusion of the coherent structure. We did not perform a study of horizontally translating vortices closer to the surface than $z_c/a_0 = -7.5$ so the behavior of Ξ/g for such physical cases is unclear. Figure 6(b) shows the same for a range of simulation parameters Re, Fr^2, We, Γ_0 and a_0. Note in this figure that the boundary between entraining and non-entraining events is not well defined as multiple parameters influence this behavior. The linear trend in Ξ/g persists for significant depth z_c/a and Ξ/g for most cases. Based on figure 6(a), for simplicity, we choose $z_c/a = -6$, or effectively 3 coherent structure diameters below the interface, to develop the model. This choice is somewhat arbitrary and a model could conceivably be constructed with variable z_c/a due to the linear trend observed in the data.

4.3. *Development of the explicit entrainment volume model*

To formally construct (4.2), we selected 60 representative DNS cases from §3 to develop respectively the functions $\mathcal{B}$, $\mathcal{F}$ and $\mathcal{W}$. We then estimate any relevant critical values from the resulting functions. The critical values presented in this section are estimates based on the DNS data and only apply to this model. When evaluated at $z_c/a = -6$ these cases obtain the following parameter ranges for model development: $240 \lesssim Re_\Gamma \lesssim 1640$, $0.3 \lesssim Fr_\Xi^2 \lesssim 4$, and $40 \lesssim We_\Gamma \lesssim \infty$.

Figure 7(a) shows average initial entrainment volume $\overline{\forall}_o$ as a function of Re_Γ at $z_c/a = -6$ for a set of simulations with variable Re, Fr^2, and $We = \infty$. Note that in this figure, $\overline{\forall}_o$ is scaled by Fr_Ξ^2. We observe a similar trend for dependence on Re_Γ as in figure 5(a) in that $\overline{\forall}_o \propto Re_\Gamma$, and viscous effects become less important for greater Re_Γ. Based on these observations, we obtain a general fit for $\mathcal{B}(Re_\Gamma; \frac{z_c}{a} = -6)$ given by:

$$\mathcal{B}(Re_\Gamma; \frac{z_c}{a} = -6) = \begin{cases} 0 & Re_\Gamma \lesssim 70 \\ c_0^v + c_1^v Re_\Gamma + c_2^v Re_\Gamma^2 & 70 \lesssim Re_\Gamma \lesssim 2580 \\ \mathcal{B}_{max} & Re_\Gamma \gtrsim 2580 \end{cases} . \tag{4.3}$$

Using the subset of the DNS data, we obtain $c_0^v = -3.39 \cdot 10^{-3}$, $c_1^v = 5.06 \cdot 10^{-5}$ and $c_2^v = -9.79 \cdot 10^{-9}$. The maximum value $\mathcal{B}_{max}$=0.062. The R^2 value for this fit to the DNS is 0.97. We estimate the range $70 < Re_\Gamma < 2580$ from the minimum root and maximum value of the function. Thus, for this z_c/a, we expect that entrainment should not occur below this Re_Γ range and should be almost independent of viscous effects above this range. Note that the quadratic fit (4.3) is quite robust and performs more satisfactorily than, say, a piece-wise linear fit with a transition at $Re_\Gamma \approx 1000$.

Figure 7(b) shows $\overline{\forall}_o$ as a function of Fr_Ξ^2 with $We = \infty$. Note that we have used (4.3) to factor out viscous effects in $\overline{\forall}_o$. The resulting dependence on Fr_Ξ^2 is close to linear with a minimum critical value $Fr_{\Xi cr}^2$ and no observed upper bound in the subset of DNS data considered. Thus, we propose as a model:

$$\mathcal{F}(Fr_\Xi^2; \frac{z_c}{a} = -6) = \begin{cases} 0 & Fr_\Xi^2 \lesssim Fr_{\Xi cr}^2 \\ c_0^c + c_1^c Fr_\Xi^2 & \text{otherwise} \end{cases} . \tag{4.4}$$

From the same subset of DNS data, we obtain $c_0^c = -0.43$, $c_1^c = 1.22$ with an R^2 value of 0.95. The linear fit provides the critical value of $Fr_{\Xi cr}^2 \approx 0.4$. Similar to the bounds found in (4.3), the model predicts no entrainment below this $Fr_{\Xi cr}^2$ for this z_c/a.

Finally, figure 7(c) shows $\overline{\forall}_o$ as a function of We_Γ for a set of cases with $Bo_\Gamma < 50$, where we estimate surface tension is relevant (based on the entire DNS data set and illustrated in figure 5(b)); and we have used both (4.3) and (4.4) to factor out the effects of viscosity and circulation flux. We observe a linear dependence between $\overline{\forall}_o$ and We_Γ and determine the following relationship:

$$\mathcal{W}(We_\Gamma; \frac{z}{a} = -6) = \begin{cases} 0 & Bo_\Gamma < 1 \\ c_0^s + c_1^s We_\Gamma & 1 < Bo_\Gamma < 50 \\ 1 & \text{otherwise} \end{cases} , \tag{4.5}$$

where based on DNS, we have used $Bo_\Gamma = 1$ as the lower limit for air entrainment. Fitting using the subset DNS obtains $c_0^s = 1.47 \cdot 10^{-2}$ and $c_1^s = 8.06 \cdot 10^{-5}$ with R^2=0.96.

Using the model (4.2) with (4.3), (4.4) and (4.5) to calculate the predicted $\forall^m$, figure 7(d) compares the model prediction against the DNS predictions for the 60 cases. The normalized root mean-square error we obtain is nRMSE=0.031. To verify that the model developed is sufficient and robust, we used the remaining (~40) cases of §3 for *a posteriori* model assessment. The overall model performance for DNS datasets now covering the parameter ranges: $110 \lesssim Re_\Gamma \lesssim 1060$, $0 \lesssim Fr_\Xi^2 \lesssim 13$, and $40 \lesssim We_\Gamma \lesssim \infty$, remains excellent (see figure 7(d)).

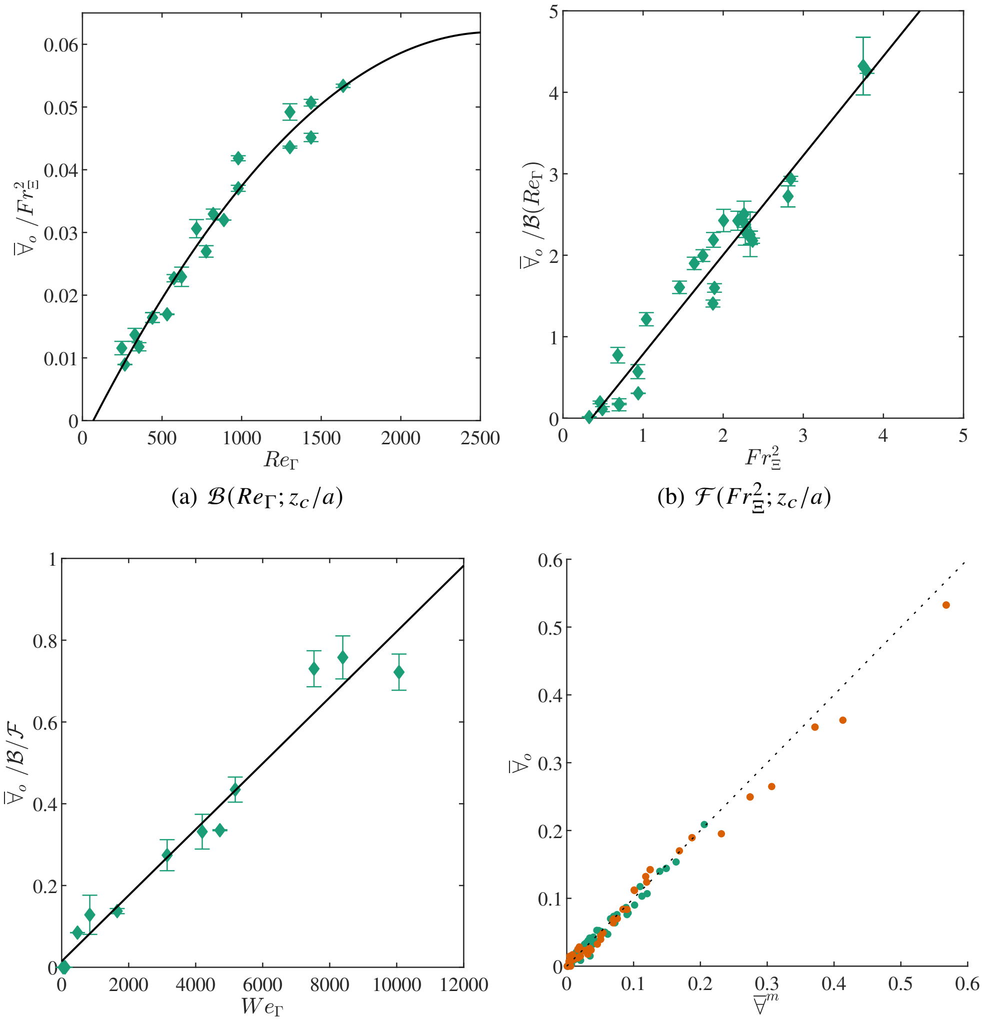

(a) $\mathcal{B}(Re_\Gamma; z_c/a)$ (b) $\mathcal{F}(Fr_\Xi^2; z_c/a)$

(c) $\mathcal{W}(We_\Gamma; z_c/a)$ (d) $\forall^m$

Figure 7: (a-c) Model functions (4.3)-(4.5) with measured average initial entrainment $\overline{\forall}_o$ for the properties at $z_c/a = -6$. (d) Comparison of predicted entrainment $\forall^{model}$ with measured average initial entrainment $\overline{\forall}_o$. • model development cases; • *a posteriori* cases not used in the model development.

5. Performance of the entrainment volume model for a more general problem

In §4, we show that the entrainment volume parameterization and model perform quite well over a broad range of the underlying physical parameters for the canonical case of a rectilinear surface-parallel vortex approaching a free surface. As an illustration of the application of this model, and to assess its general validity and robustness, we consider a more general and complex problem of air entrainment in the wake of a fully-submerged horizontal cylinder in a uniform flow. We choose this problem because, within an appreciable range of speeds and submergence, quasi two-dimensional surface-parallel vortex structures behind the cylinder interact with the interface leading to air entrainment. Briefly, for cylinders close to the surface, the interaction of the underlying cylinder wake and the free surface creates two types of wake structures that produces quasi-steady breaking waves or spilling jet flows near the first trough of the wave system behind the cylinder (e.g., Sheridan *et al.* 1995, 1997; Reichl *et al.* 2005; Colagrossi *et al.* 2019). Although not explicitly addressed in these studies, wave breaking and associated entrainment is implied. For deeper cylinders, we observed both types of wake structures depending upon the cylinder Froude number (Hendrickson & Yue 2019*a*). For large cylinder Froude numbers, we observed a turbulent bore-like region riding the front face of the first wave behind the cylinder similar to that observed behind streamlined objects (Duncan 1981, 1983) and found no correlation between the entrainment signal and the underlying cylinder wake. For small cylinder Froude numbers, we observed periodic plunging breaking events at the first wave crest and determined that the measured frequency of entrainment correlated with the cylinder-wake Strouhal number. It is within this parameter range that we assess the predictions of the model.

We use a similar DNS described in §3 with a Boundary Data Immersion Method (BDIM) (Maertens & Weymouth 2015) to model the no-slip body boundary condition on the fixed cylinder surface. The method and numerical convergence results are described in detail in (Hendrickson & Yue 2019*a*). Figure 8(a) is a schematic of the simulation setup and parameters. For definiteness, we fix the cylinder center depth at $2d$ below a static water line $z = 0$, where d is the cylinder diameter. We normalize all physical quantities by length, velocity (and time) scales d, U, the uniform inflow velocity (and d/U) respectively. We neglect surface tension and focus on the low cylinder Froude number ($Fr_d = U/\sqrt{gd}$) regime we identified that produces the periodic plunging breaking events. Figures 8(b)-8(c) show an instantaneous visualization of a individual entrainment event for a representative simulation at Reynolds number $Re_d = Ud/\nu_w$=250. The sequence shows an individual entrainment event, which occurs on the first wave behind the cylinder, in relation to a wide view of the transverse vorticity field. In this sequence, the plunging breaker forms, plunges, entrains air and resets. This event repeats with a frequency that correlates with the measured cylinder wake Strouhal number (Hendrickson & Yue 2019*a*). Figure 9(a) shows a sample plot of the entrainment volume as a function of time. The periodicity of the entrainment events correlates with the cylinder-wake Strouhal number for all cases used in this analysis.

5.1. *Analysis of DNS data for the cylinder wake entrainment problem*

We apply the analysis of §2.2 and §4 to the vortical air-entraining flow behind the fully-submerged cylinder. This section provides an overview of the analysis process and steps taken to assess and reduce, where necessary, sensitivity of the estimates we obtain.

First, we measure the total entrainment volume of the n-the entrainment event as $\mathcal{V}_e^{(n)} = \mathcal{V}_e(t_e^{(n)}) - min(\mathcal{V}_e(t_e^{(n-1)} : t_e^{(n)}))$, where $t_e^{(n)}$ is the time of the n-th local peak in the total entrainment volume (cf. figure 9(a)). We include only the initial (largest) peaks, neglecting smaller secondary entrainment measurements close to the initial event in keeping with the macroscopic framework. The average entrainment volume for N_e events is $\overline{\mathcal{V}_e} = (\Sigma_n \mathcal{V}_e^{(n)})/N_e$. Figure 9(b) shows the average entrainment volume as a function of cylinder Froude number, with the 95% confidence value bar based on the standard deviation. The entrainment volume scales linearly with cylinder Froude number (as noted in Hendrickson & Yue (2019*a*)).

Second, to identify the coherent structures in the flow field, we must choose a value of λ_{cr} to identify and quantify the coherent vortex structures, as discussed in §2.2. The value of λ_{cr} generally determines the size and extent of the identified vortex structure, with the threshold enstrophy scaled by $|\omega|^2 \gtrsim -4\lambda_{cr}$ (Jeong & Hussain 1995). For the current problem, we find that the cylinder wake is not captured well for $\lambda_{cr} \lesssim -15$, while for $\lambda_{cr} \gtrsim -5$ the resulting vortex structures are large and diffused. Thus we consider effect of variations in λ_{cr} centered

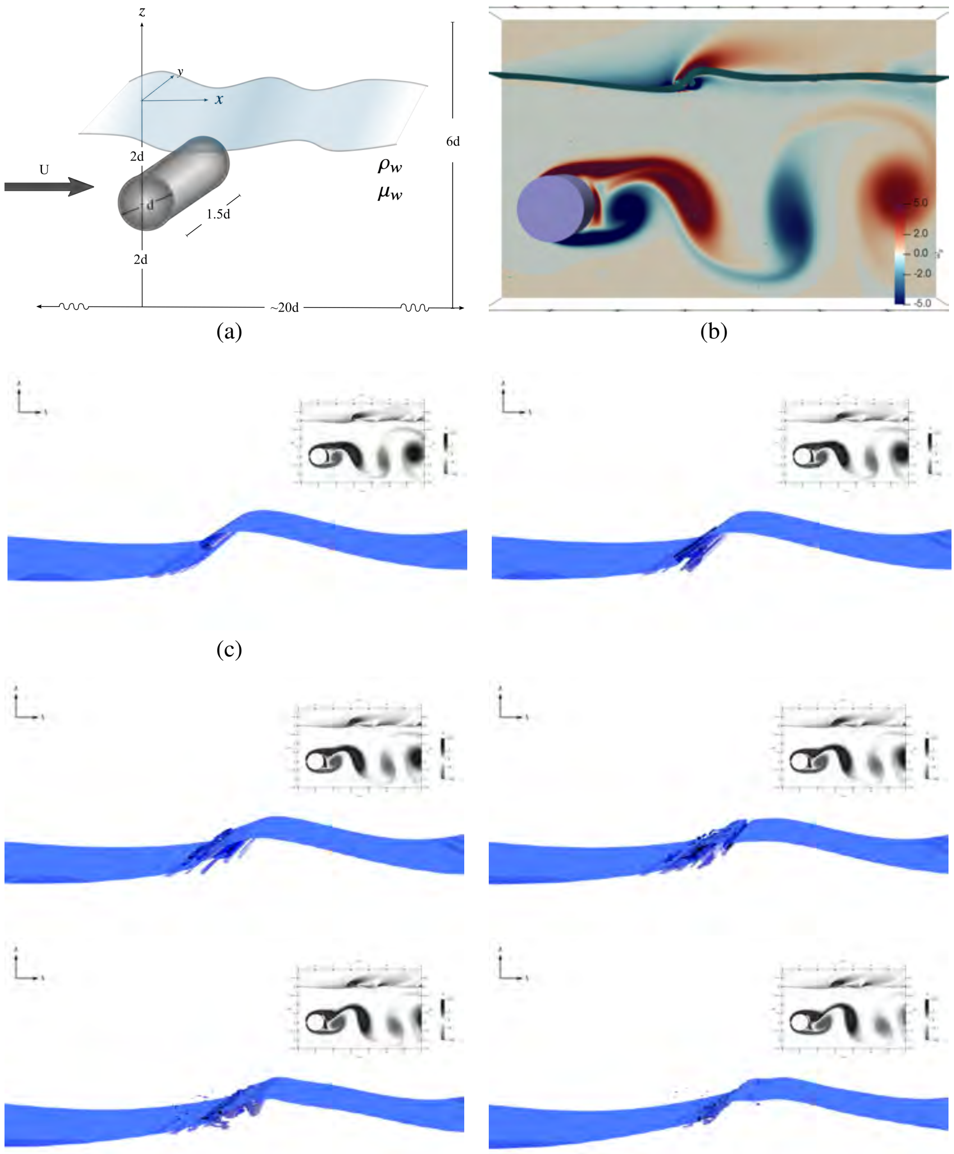

Figure 8: (a) A schematic for DNS of a flow past a fully-submerged cylinder; (b) center-plane instantaneous transverse vorticity contours ω_y and air-water interface; and (c) close up visualization of individual entrainment event with blue isosurface f=0.5 and purple $\lambda_2 = -10$ for $f \geqslant 0.5$ with a representative vertical plane transverse vorticity (inset). Cylinder DNS parameters: Re_d=250 and $Fr_d^2 = 0.27$.

around $\lambda_{cr} = -10$ and assess the sensitivity in the model prediction. Overall, we find that varying λ_{cr} in the range $-12 \leqslant \lambda_{cr} \leqslant -8$ resulted in a (general) change in average structure volume of 17-10% relative to $\lambda_{cr} = -10$. More details on the overall sensitivity of the model performance to the value of λ_{cr} appear in §5.2.

Third, unlike the laminar vortex pair dataset, it is necessary to estimate the local effective viscosity in the mixing region behind the cylinder containing the coherent vorticity (for

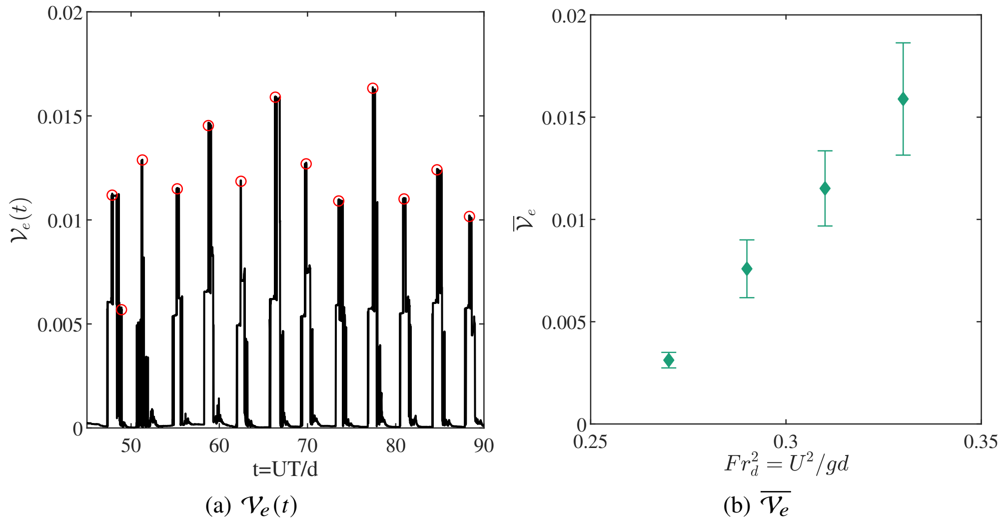

Figure 9: DNS of a fully submerged cylinder: (a) Total entrainment volume as a function of time for Fr_d^2=0.31 and Re_d=250; ∘ $\mathcal{V}_e(t_e^n)$. (b) Average entrainment as a function of Fr_d^2 for Re_d=250 with 95% confidence error bars.

obtaining Re_Γ in the model) as we expect the Reynolds number and turbulent viscosity to increase along the streamwise direction (e.g., Pope 2000). To do this, we use a technique from iLES (Aspden *et al.* 2008; Hendrickson *et al.* 2019) that calculates $\nu_{\text{eff}} = \overline{\epsilon/\mathcal{D}}$ within a control volume. Here, ϵ is the (negative) time rate of change of the kinetic energy $\rho_w \vec{u} \cdot \vec{u}/2$ in the control volume, accounting for the appropriate fluxes in and out of the volume, and $\mathcal{D} = V^{-1} \int \vec{u} \cdot \nabla^2 \vec{u} dV$ represents the work done by diffusion. To ensure that the control volume is sufficiently large to contain the coherent structure of interest, we select the control volume V as $2 < x/d < 3$ and $-2.5 < z/d < -1.5$ to include the vertical extent of the cylinder near the observed breaking events. Using this, we obtain $860 < \nu_{\text{eff}}^{-1} < 870$ for the four cases in figure 9(b). An extensive sensitivity analysis on the effect of the domain and size of the V show that ν_{eff} changes by less than 0.6% with a 5% change in V.

Finally, we identify which (if any) of the coherent vortex structures found in the cylinder wake correlates with an observed entrainment event. To do this, we develop an event-by-event analysis technique that is free from subjective bias. Between entrainment events $t_e^{(n-1)} < t < t_e^{(n)}$, we first bin the identified structures by their location behind the cylinder and assess whether they meet the criteria developed in section §4.3 — namely a positive circulation flux and centroid locations $-7 < z_c/a < -4$ below the static water line. We observe that the coherent vortex structures shed from the lower portion of the cylinder always meet the criteria when $x/d > 1$, and we use this subset of the coherent structures for further analysis.

5.2. *Model Predictions for Entrainment in Cylinder Wake*

Using data analysis outlined in §5.1, we identify the coherent vortex structures and estimate the associated model parameters for each n-th entrainment event (across the four cylinder cases, the total number events is 37). Figure 10(a) shows the resulting $Re_\Gamma^{(n)} = |\Gamma|^{(n)}/\nu_{\text{eff}}$ and z_c/a using $\lambda_{cr} = -10$. For all of the events, the relative vortex centroid depth below the static waterline has an average value of $z_c/a = -6.4$, thus enabling us to use (4.3)-(4.4)

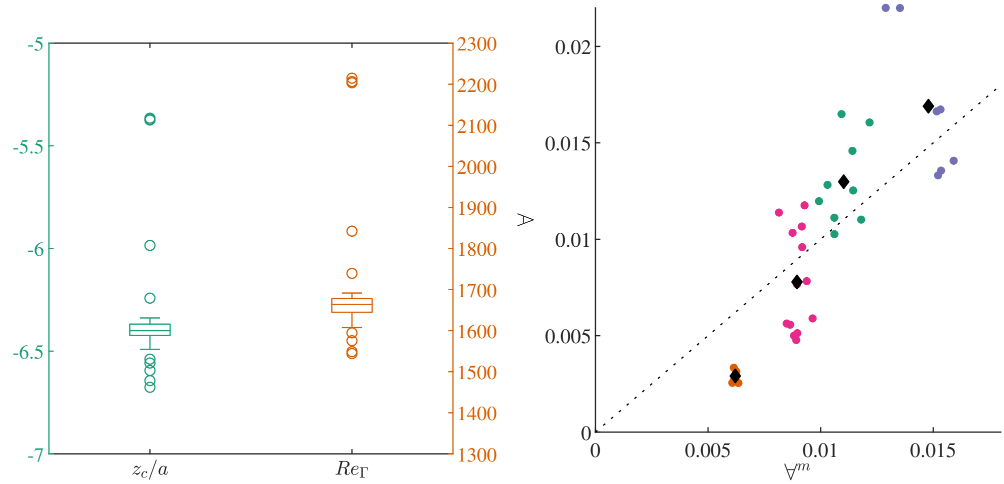

(a) (b)

Figure 10: (a) Whisker plot of $(z_c/a)^{(n)}$ and $Re_\Gamma^{(n)} = |\Gamma|^{(n)}/\nu_{eff}$ for all entrainment events (all cylinder cases). (b) Comparison of predicted entrainment $\forall^m$ from (4.2)–(4.5) with measured entrainment $\forall$. In (b) for reference: Fr_d^2 =(● 0.27; ● 0.29; ● 0.31; ● 0.33); ♦ average value for each Fr_d^2 case; and - - - $\forall = \forall^m$. $\lambda_{cr} = -10$

without modification. For reference, the average (effective) circulation Reynolds number is 1664 and all entrainment events fall within the range of (4.3) where Reynolds number is a factor in the entrainment volume prediction.

Figure 10(b) shows a comparison of the normalized observed event entrainment volume $\forall = \mathcal{V}_e^{(n)}/V_{\lambda 2}^{(n)}$ and the predicted entrainment volume using (4.2)–(4.5). The normalized RMSE for all of the events is nRMSE=0.175 (RMSE=0.0035). For information, we indicate the Fr_d^2 of each event and include an average estimate for each Fr_d^2 case with $\overline{Re_\Gamma} = N_e^{-1}\Sigma_n \Gamma^{(n)}/\nu_{\text{eff}}$, $\overline{Fr_\Xi^2} = N_e^{-1}\Sigma_n (Fr_\Xi^2)^{(n)}$ and $\overline{\forall} = N_e^{-1}\Sigma_n \forall^{(n)}$. The normalized RMSE is nRMSE=0.162 (RMSE=0.0023) using these average quantities. These results are for $\lambda_{cr} = -10$. As previously noted, the model prediction is somewhat sensitive to this value of λ_{cr}. For $-12 \leqslant \lambda_{cr} \leqslant -8$, the nRMSE over all events varies between 0.18 and 0.21, not significantly different from the $\lambda_{cr} = -10$ baseline model prediction. Despite the differences between this problem and the model development problem in §3 (such as the presence of weak free-surface turbulence and a strong convective inflow velocity), the macroscopic framework satisfactorily predicts the initial entrainment volume that correlates with the large vortex structures behind the cylinder. This indicates that the key dimensionless parameters we identified, namely Fr_Ξ^2 and Re_Γ, and the functional dependence of entrainment on them, provide a useful model for air entrainment by large-scale, surface-parallel coherent vortical structures.

6. Summary

We perform direct numerical simulations (DNS), data analysis, and macroscopic entrainment event modeling of the initial entrainment volume due to the interaction of a rectilinear surface-parallel vortex rising towards an air-water interface. For the general case, we develop a coherent structure identification scheme to estimate and quantify the vortex geometric and kinematic quantities. These include the circulation Γ of the primary horizontal vorticity, equivalent radius a, and vertical rise velocity W.

As a canonical problem, we consider the air entrainment by a surface-parallel coherent vortex structure rising toward the free surface as part of a rectilinear vortex pair. For this problem we perform systematic three-dimensional DNS of the incompressible, two-phase Navier-Stokes equations over broad ranges of physical parameters — Froude, Weber and Reynolds numbers; as well as vortex radius a, vortex pair separation ℓ and orientation angle Θ (which affects the rise velocity W). Based on the extensive DNS data we generated for this problem, we obtain the key parameterization for the air entrainment volume. We identify a new parameter, the circulation flux Froude number $Fr_{\Xi}^2 = \Xi/g$ which measures the relative importance of the circulation flux $\Xi \equiv \Gamma W/a^2$ to gravity g, and controls the air volume entrained. We show that it is the most important parameter governing the total volume of air entrained.

We propose a simple, phenomenological model for the entrainment volume expressed as the product of three factors representing the separate effects of Fr_{Ξ}^2, the circulation Weber number $We_\Gamma = \Gamma^2(a(\sigma/\rho_w))^{-1}$, and the circulation Reynolds number $Re_\Gamma = |\Gamma|/\nu_w$, all defined/estimated at some distance z_c/a below the free surface. The model performs extremely well over a broad range of these parameters for the vortex pair DNS cases.

To assess the usefulness and robustness of the new model, we apply it to a more general and complex problem of air entrainment by the horizontal vorticity shed from a submerged circular cylinder in uniform flow. We focus on and perform DNS for the range of cylinder Froude number characterized by large horizontal coherent vortical structures in the wake and quasi-periodic wave breaking and air entrainment on the surface. Using a general vorticity identification scheme to obtain the model parameters for the coherent horizontal vorticity structures and kinematics, the phenomenological model performs satisfactorily compared to DNS of the cylinder problem.

Our main interest in this work is predicting the total entrained volume in the context of a macroscopic event framework rather than the detailed structures and mechanisms of the vortex-interface interactions. In this context, we have focused on macroscopic air entrainment events associated with coherent structures with primarily surface-parallel vorticity aligned in a dominant direction. Despite these restrictions, such scenarios are common, for example, in air entrainment in large Froude number (isotropic) free-surface turbulence (see, e.g., Yu *et al.* 2019*a*) and vertically immersed flat-plate boundary layers (Masnadi *et al.* 2019). Our hypothesis that a phenomenological model based on macroscopic parameterization of the vortical structure can capture the subsequent entrainment volume has guided and simplified the current approach and modeling for the types of interactions studied here. This work identifies the key parameters necessary for macroscopic entrainment modeling for large-scale computations where high-fidelity flow data is unavailable. An immediate application, for example, is to obtain predictions using the present model of the entrainment volume in a ship wake, based on resolved flow quantities obtained from large-scale uRANS calculations. Such predictions, when compared to available measurements, can provide an assessment of the validity and applicability of the present model. This work is now underway.

Acknowledgments. This work was funded by the Office of Naval Research N00014-20-2059 under the guidance of Dr. W.-M. Lin. The computational resources for the effort were funded through the High Performance Computing Modernization Program at the Department of Defense. The authors wish to thank Prof. Pablo Carrica for the useful discussions in preparation of this manuscript.

Declaration of Interests. The authors report no conflict of interest.

Author ORCID. K. Hendrickson, https://orcid.org/0000-0002-3596-6556; D. Yue, https://orcid.org/0000-0003-1273-9964

Appendix A. DNS of entrainment by a surface-parallel vortex pair near an air-water interface

The interaction of a horizontal vortex pair with a free surface in the absence of entrainment is well documented (Sarpkaya 1996; Rood 1994*b*,*a*, 1995; Sarpkaya & Suthon 1991; Ohring & Lugt 1991; Yu & Tryggvason 1990; Dommermuth 1993). This appendix verifies our simulations for non-entraining vortex behavior and highlights the differences of the behavior when entrainment occurs.

A.1. *Verification of non-entraining vortex behavior*

Each column of figure 11 shows a sequence of instantaneous vorticity contours for different Fr^2 and We and at increasing time instances during the evolution. The non-dimensional entrainment volume $\overline{\forall}_o = \mathcal{V}_e/(L_y \pi a_0^2)$ increases from left to right, $\overline{\forall}_o = (0.0, 0.013, 0.097)$. The bottom row represents the corresponding vortex motion of the two strongest vortices in the water (as identified using the method in §2.2 with $\lambda_{cr} = 0$). As the primary (positive) vortex rises towards the interface, the surface deforms and secondary (negative) vorticity forms in both fluids at the surface due to interface curvature and the presence of viscosity (Rood 1994*b*,*a*, 1995; Orlandi 1990). If the secondary vorticity is strong enough (columns 2 and 3), it couples with the primary vortex and this new pair (of unequal strengths) process around each other via mutual induction (Ohring & Lugt 1991; Orlandi 1990). In column 1, surface tension sufficiently suppresses the surface curvature such that no significant coupling occurs and the primary vortex follows a path similar to the classical solution of the path of an inviscid point vortex near a wall (Lamb 1932). Our simulations showed that the primary vortex path will always approach this classical solution when Froude number is reduced or surface tension restricts the surface motion. This finding is consistent with the viscous simulations of Ohring & Lugt (1991) and the inviscid simulations of Yu & Tryggvason (1990).

A.2. *Vortex behavior for entrainment cases*

Columns 2 and 3 of figure 11 include entrainment events. In both cases, the entrained air generally tracks with the secondary vortex as the coupled pair retreats deeper into the water bulk. For larger Fr^2 (column 3), multiple secondary vortices appear in the water implying that the vortex procession involves three or more vortex structures, resulting in increased entrainment volume.

A survey of our simulations show that the coupling of the vortices and the procession of the secondary vorticity into the bulk can correlate with entrainment. Figure 12 shows the path of the primary vortex center for a range of Fr^2 and We. First, we note that the gravity has a much stronger influence on the primary vortex approach to the surface compared to surface tension, as indicated by the point at which the vortex motion transitions from vertical to horizontal. Second, the return of the primary vortex into the water bulk (below the classical theory line) indicates stronger secondary surface vorticity and coupling. The steeper the return of the primary vortex to the bulk, the stronger the coupling and the resulting entrainment. However, as shown by Ohring & Lugt (1991) and confirmed in the vortex paths in figures 11 and 12, this event is not a sufficient indicator for entrainment by itself. What our simulations do show is that this coupling and procession is likely responsible for the transport of air to the bulk.

We summarize briefly the vortex behavior for the oblique cases using $\Theta = \pi/4$ as an illustration in figure 13. The vortex pair rises obliquely to the interface consistent with the orientation angle and the surface deforms due to the influence of vortex 1 (the positive vortex closes to the interface at $t = 0$). This generates secondary negative vorticity at the interface. Vortex 1 turns away from inclination axis, as expected by the classical theory and shown in

Lugt & Ohring (1994). As in the $\Theta = 0$ case, if the secondary surface vorticity near vortex 1 is strong enough, they will couple and process downward into the bulk. After vortex 1 couples to its secondary surface vorticity, the contours representing vortex 2 become circular and it continues its approach to the surface following the original rise angle. In all cases considered, the surface deformation associated with vortex 2 is significantly less but can also cause entrainment. In our simulations we focused on entrainment events by vortex 1 only and observed entrainment for all angles $\Theta < 75°$ at the initial depth studied.

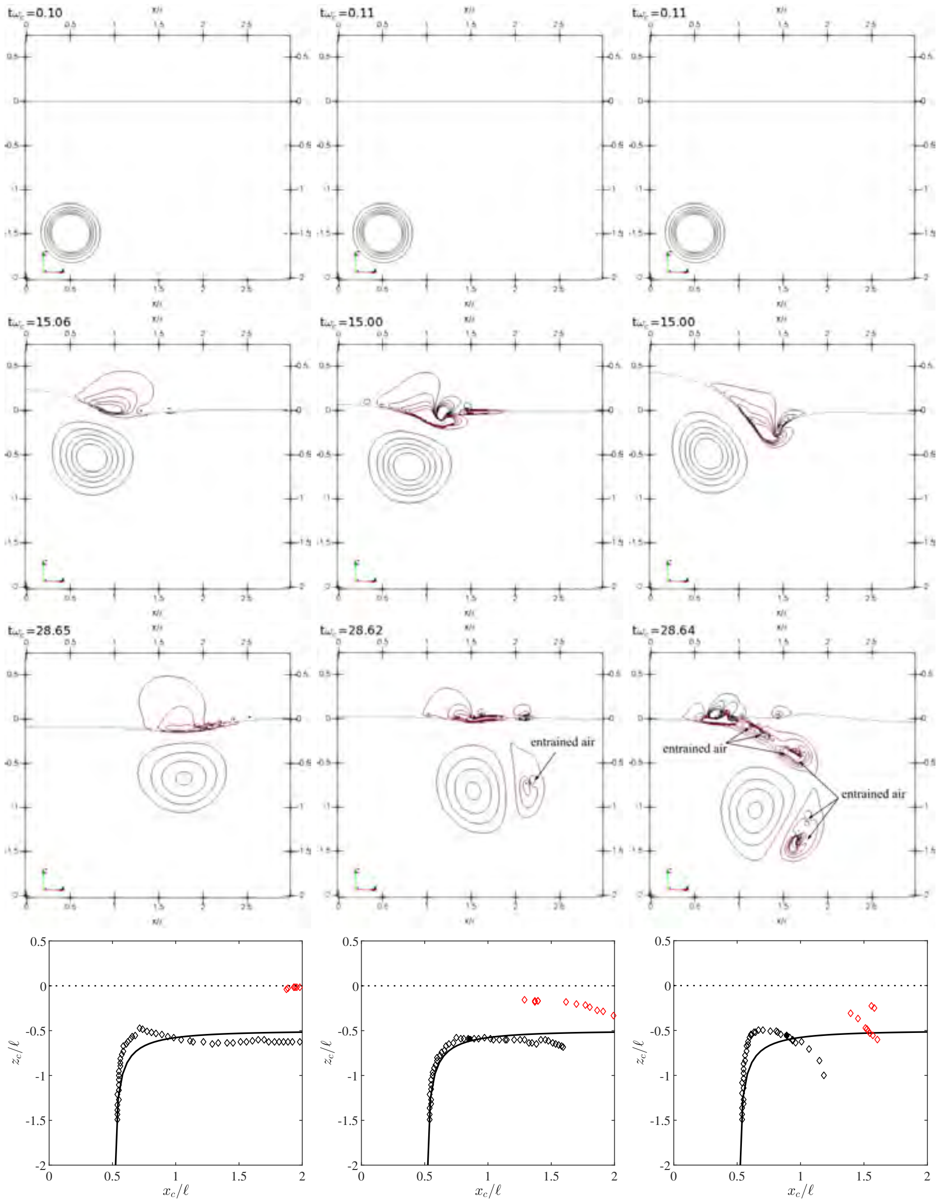

Figure 11: Contours of transverse vorticity ω_y/ω_c (—— ω_y<0) on the center-plane for Re = 628 ℓ/a_0=5; for (Fr^2, We) = (790, 99) (left); (197, ∞) (center); and (790, ∞) (right); for increasing time instances in the evolution (top 3 rows). Vorticity bounds are −1.5, 1.5. Black line near z = 0 is interface. Bottom row: Primary vortex path for ◇ $\omega_y > 0$ and ◇ $\omega_y < 0$ with — Lamb (1932) and - - - z = 0.

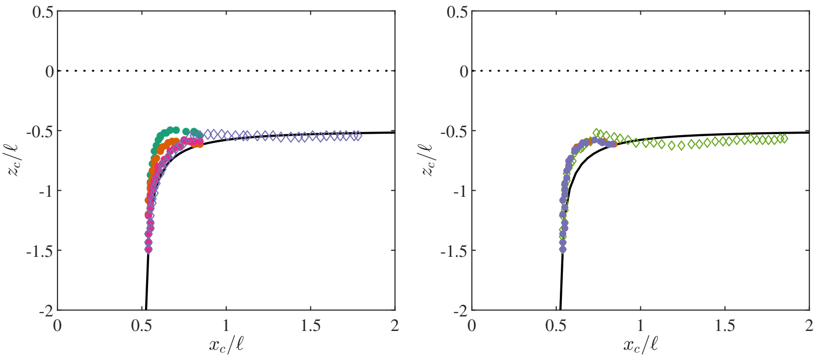

(a) Fr^2=(♦ 790;♦ 493; ♦ 197; ◇ 99) and We=∞

(b) Bo=(♦ ∞; ♦ 4; ◇ 0.2) and Fr^2=494.

Figure 12: Primary vortex path prior to entrainment onset (if entraining) $t < t_{\text{onset}}$ for $Re = 628$ and $\ell/a_0 = 5$. Filled symbols are entraining cases. —— Lamb (1932); - - - $z = 0$.

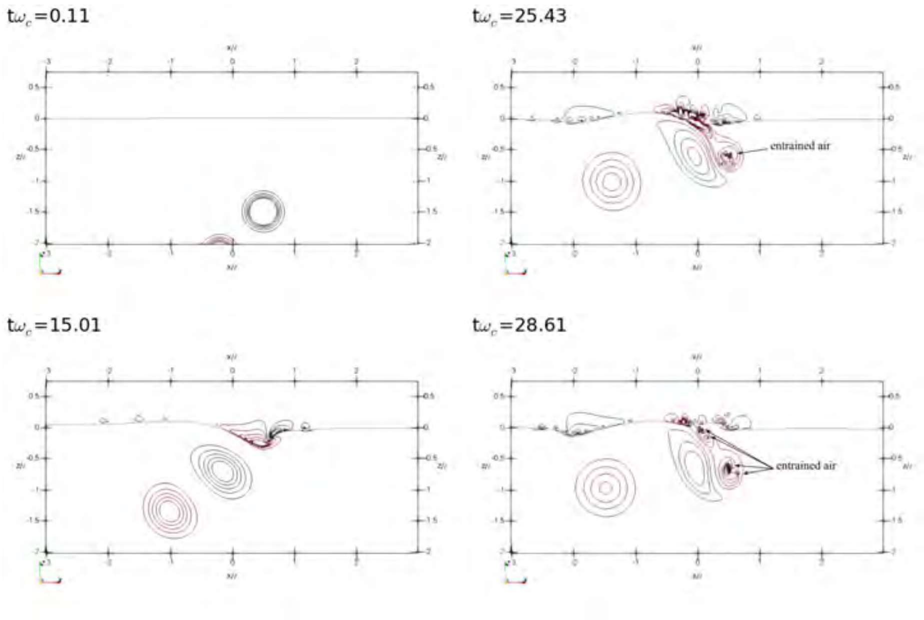

Figure 13: Contours of transverse vorticity ω_y/ω_c (—— ω_y<0) on the center-plane for an oblique incidence angle $\Theta = \pi/4$ with ℓ/a_0=5, Fr^2 = 494, Re = 628 and We = ∞. Time evolution is top-down, left-right. Red contours are negative vorticity. Vorticity bounds are −1.5, 1.5. Black line near $z = 0$ is interface.

REFERENCES

André, M. A. & Bardet, P. M. 2017 Free surface over a horizontal shear layer: vorticity generation and air entrainment mechanisms. *J. Fluid Mech.* **813**, 1007–1044.

Aspden, A., Nikiforkakis, N., Dalziel, S. & Bell, J. B. 2008 Analysis of implicit LES methods. *Comm. App. Math. and Comp. Sci.* **3** (1), 103–126.

Baldy, S. 1993 A generation-dispersion model of ambient and transient bubbles in the close vicinity of breaking waves. *J. Geophys. Res* **98** (C10), 18277–18293.

Biń, A. K. 1993 Gas entrainment by plunging liquid jets. *Chem. Eng. Sci* **48** (21), 3585–3630.

Brackbill, J. U., Kothe, D. B. & Zemach, C. 1992 A continuum method for modeling surface tension. *J. Comp. Phys.* **100** (2), 335–354.

Campbell, B. K., Hendrickson, K. & Liu, Y. 2016 Nonlinear coupling of interfacial instabilities with resonant wave interactions in horizontal two-fluid plane Couette-Poiseuille flows: Numerical and physical observations. *J. Fluid Mech.* **809**, 438–479.

Castro, A. M., Li, J. & Carrica, P. M. 2016 A mechanistic model of bubble entrainment in turbulent free surface flows. *Int. J. Multiph. Flow* **86**, 35–55.

Chan, W.-H. R., Dodd, M S., Johnson, P L. & Moin, P 2021 Identifying and tracking bubbles and drops in simulations: a toolbox for obtaining sizes, lineages, and breakup and coalescence statistics. *J. Comp. Phys.* **432**, 110156.

Colagrossi, A, Nikolov, G, Durante, D, Marrone, S & Souto-Iglesias, A 2019 Viscous flow past a cylinder close to a free surface: Benchmarks with steady, periodic and metastable responses, solved by meshfree and mesh-based schemes. *Comput. Fluids* **181**, 345–363.

Crow, S. C. 1970 Stability theory for a pair of trailing vortices. *AIAA J.* **8** (12), 2172–2179.

Deane, G B & Stokes, M D 2002 Scale dependence of bubble creation mechanisms in breaking waves. *Nature* **418** (6900), 839–844.

Derakhti, M. & Kirby, J. T. 2014 Bubble entrainment and liquid-bubble interaction under unsteady breaking waves. *J. Fluid Mech.* **761**, 464–506.

Dommermuth, D. G. 1993 The laminar interactions of a pair of vortex tubes with a free surface. *J. Fluid Mech.* **246**, 91–115.

Drazen, D. A., Fullerton, A. M., Fu, T. C., Beale, K. L.C., O'Shea, T. T., Brucker, K. A., Dommermuth, D. G., Wyatt, D. C., Bhushan, S., Carrica, P. M. & Stern, F. 2010 A comparison of model-scale experimental measurements and computational predictions for a large transom-stern wave. In *Proceedings of the 28th Symposium on Naval Ship Hydrodynamics*.

Duncan, J. H. 1981 An experimental investigation of breaking waves produced by a towed hydrofoil. *Proc. R. Soc. Lond. A Math. Phys. Sci.* **377** (1770), 331–348.

Duncan, J. H. 1983 The breaking and non-breaking wave resistance of a two-dimensional hydrofoil. *J. Fluid Mech.* **126**, 507–520.

Ezure, T., Kimura, N., Miyakoshi, H. & Kamide, H. 2011 Experimental investigation on bubble characteristics entrained by surface vortex. *Nucl. Eng. Des* **241** (11), 4575–4584.

Falgout, R. D., Jones, J. E. & Yang, U. M. 2006 The design and implementation of *hypre*, a library of parallel high performance preconditioners. In *Numerical Solution of Partial Differential Equations on Parallel Computers*, pp. 267–294. Springer-Verlag.

Fu, T. C., Fullerton, A. M., Terrill, E. J. & Lada, G. 2006 Measurements of the wave fields around the R/V Athena I. In *Proceedings of the 26th Symposium on Naval Ship Hydrodynamics*.

Hendrickson, K., Weymouth, G.D. & Yue, D.K.-P. 2020 Informed component label algorithm for robust identification of connected components with volume-of-fluid method. *Comput. Fluids* **197**, 104373.

Hendrickson, K., Weymouth, G. D., Yu, X. & Yue, D. K.-P. 2019 Wake behind a three-dimensional dry transom stern. Part 1: Flow structure and large-scale air entrainment. *J. Fluid Mech.* **875**, 854–883.

Hendrickson, K. & Yue, D. K.-P. 2019*a* Structures and mechanisms of air-entraining quasi-steady breaking ship waves. *J. Ship Res.* **63** (2).

Hendrickson, K & Yue, D K.-P. 2019*b* Wake behind a three-dimensional dry transom stern. Part 2: Analysis and modeling of incompressible highly-variable density turbulence. *J. Fluid Mech.* **875**, 884–913.

Hunt, J.C.R., Wray, A. & Moin, P. 1988 Eddies, stream, and convergence zones in turbulent flows. *Tech. Rep.*. Center for Turbulence Research Report CTR-S88.

Jeong, J. & Hussain, F. 1995 On the identification of a vortex. *J. Fluid Mech.* **285**, 69–94.

Klettner, C. A. & Eames, I. 2012 Momentum and energy of a solitary wave interacting with a submerged semi-circular cylinder. *J. Fluid Mech.* **708**, 576–595.

Lamb, H. 1932 *Hydrodynamics*, 6th edn. New York: Dover Publications.

Leng, X. & Chanson, H. 2019 Two-phase flow measurements of an unsteady breaking bore. *Exp. Fluids* **60** (3), 1–15.

Lugt, H. J. & Ohring, S. 1992 The oblique ascent of a viscous vortex pair toward a free surface. *J. Fluid Mech.* **236** (461), 461–476.

Lugt, H. J. & Ohring, S. 1994 The oblique rise of a viscous vortex ring toward a deformable free surface. *Meccanica* **29**, 313–329.

Ma, G., Shi, F. & Kirby, J. T. 2011 A polydisperse two-fluid model for surf zone bubble simulation. *J. Geophys. Res* **116** (5).

Maertens, A. P. & Weymouth, G. D. 2015 Accurate Cartesian-grid simulations of near-body flows at intermediate Reynolds numbers. *Comput. Methods in Appl. Mech. Eng.* **283**, 106–129.

Masnadi, N., Erinin, M. A., Washuta, N., Nasiri, F., Balaras, E. & Duncan, J. H. 2019 Air entrainment and surface fluctuations in a turbulent ship hull boundary layer. *J. Ship Res.* **63** (4), 1–17.

Ohring, S. & Lugt, H. J. 1991 Interaction of a viscous vortex pair with a free surface. *J. Fluid Mech.* **227**, 47–70.

Orlandi, P. 1990 Vortex dipole rebound from a wall. *Phys. Fluids* **2** (8), 1429–1436.

Pope, S. B 2000 *Turbulent Flows*. Cambridge Univ. Press, Cambridge, UK.

Popinet, S. 2009 An accurate adaptive solver for surface-tension-driven interfacial flows. *J. Comp. Phys.* **228**, 5838–5866.

Popinet, S. 2018 Numerical Models of Surface Tension. *Annu. Rev. Fluid Mech.* **50**, 49–75.

Reichl, P., Hourigan, K. & Thompson, M. C. 2005 Flow past a cylinder close to a free surface. *J. Fluid Mech.* **533**, 269–296.

Rood, E. P. 1994*a* Interpreting vortex interactions with a free surface. *J. Fluids Eng.* **116** (1), 91–94.

Rood, E. P. 1994*b* Myths, math, and physics of free-surface vorticity. *Appl. Mech. Rev.* **47** (6), S152–S156.

Rood, E. P. 1995 Vorticity interactions with a free surface. In *Fluid Vortices*, chap. 16, pp. 687–730. Springer.

Sarpkaya, T. 1996 Vorticity, Free Surface, and Surfactants. *Annu. Rev. Fluid Mech.* **28** (1), 83–128.

Sarpkaya, T. & Suthon, P. 1991 Interaction of a vortex couple with a free surface. *Exp. Fluids* **11** (4), 205–217.

Sheridan, J., Lin, J.-C. & Rockwell, D. 1995 Metastable states of a cylinder wake adjacent to a free surface. *Phys. Fluids* **7** (9), 2099–2101.

Sheridan, J., Lin, J.-C. & Rockwell, D. 1997 Flow past a cylinder close to a free surface. *J. Fluid Mech.* **330**, 1–30.

Tran, T., de Maleprade, H., Sun, C. & Lohse, D. 2013 Air entrainment during impact of droplets on liquid surfaces. *J. Fluid Mech.* **726**, R3.

Weymouth, G. D. & Yue, D. K.-P. 2010 Conservative Volume-of-Fluid method for free-surface simulations on Cartesian-grids. *J. Comp. Phys.* **229** (8), 2853–2865.

Widnall, S. E. 1975 The Structure and Dynamics of Vortex Filaments. *Annu. Rev. Fluid Mech.* **7** (1), 141–165.

Wyatt, D. C., Fu, T. C., Taylor, G. L., Terrill, E. J., Xing, T., Bhushan, S., O'Shea, T. T. & Dommermuth, D. G. 2008 A comparison of full-scale experimental measurements and computational predictions of the transom-stern wave of the R/V Athena I. In *Proceedings of the 27th Symposium on Naval Ship Hydrodynamics*.

Yu, D & Tryggvason, G 1990 The free-surface signature of unsteady, two-dimensional vortex flows. *J. Fluid Mech.* **218**, 547–572.

Yu, X. 2019 Theoretical and numerical study of air entrainment and bubble size distribution in strong free-surface turbulent flow at large Froude and Weber number. PhD thesis, Massachusetts Institute of Technology.

Yu, X., Hendrickson, K., Campbell, B. K. & Yue, D. K.-P. 2019*a* Numerical investigation of shear-flow free-surface turbulence and air entrainment at large Froude and Weber numbers. *J. Fluid Mech.* **880**, 209–238.

Yu, X., Hendrickson, K. & Yue, D. K.-P. 2019*b* Scale separation and dependence of entrainment bubble-size distribution in free-surface turbulence. *J. Fluid Mech.* **885**, R2.